

Article

A Dual-Harmonic Pole-Changing Motor with Split Permanent Magnet Pole

Yi Du ^{1,*} , Jiayan Zhou ¹, Zhuofan He ¹, Yandong Sun ² and Ming Kong ³¹ Department of Electrical Engineering, College of Engineering, Jiangsu University, Zhenjiang 212013, China² China Automotive Innovation Corporation, Nanjing 211100, China³ Zhenjiang Power Supply Company, State Grid Jiangsu Electric Power Co., Ltd., Zhenjiang 212000, China

* Correspondence: duyie@ujs.edu.cn

Abstract: This paper proposes a dual-harmonic pole-changing (PC) motor with split permanent magnet (PM) poles (DHPCM-SPMPs). By adopting a split PM pole structure, the amplitude of the third PM flux density is increased greatly. Therefore, when a PC winding is adopted to couple with the fundamental and third PM flux density components, respectively, the proposed motor can work as a PC PM motor to satisfy operating demands of electric tractors. The design and effect of the proposed split PM pole structure is introduced first. The winding topology is then designed according to the slot vector diagrams of the two PM flux density components, and the PC operation can be realized by electric switches. Aiming at a torque ratio design objective, the PM structure parameters can be determined based on mathematical derivation, and the speed-widening capability is proved based on the operation characteristic analysis. Finally, the electromagnetic performance of the DHPCM-SPMPs is investigated and compared by finite element analysis, which shows the high torque capability in eight-pole mode and the wide speed range in twenty-four-pole mode benefiting from the PC operation.

Keywords: dual-harmonic; pole-changing; speed-widening capability; split permanent magnet poles



Citation: Du, Y.; Zhou, J.; He, Z.; Sun, Y.; Kong, M. A Dual-Harmonic Pole-Changing Motor with Split Permanent Magnet Pole. *Energies* **2022**, *15*, 7716. <https://doi.org/10.3390/en15207716>

Academic Editor: Anna Richelli

Received: 24 September 2022

Accepted: 17 October 2022

Published: 19 October 2022

Publisher's Note: MDPI stays neutral with regard to jurisdictional claims in published maps and institutional affiliations.



Copyright: © 2022 by the authors. Licensee MDPI, Basel, Switzerland. This article is an open access article distributed under the terms and conditions of the Creative Commons Attribution (CC BY) license (<https://creativecommons.org/licenses/by/4.0/>).

1. Introduction

Electric tractors (ETs) possess great potential in agriculture to replace diesel tractors for the merits of non-pollution and low noise [1–3]. In order to achieve high-efficiency operation, permanent magnet (PM) synchronous motors (PMSMs), which have been adopted widely for electric vehicles, are the most competitive candidates for ETs because of the characteristics of high torque density and high efficiency [4–8]. However, ETs, as a kind of special electric vehicle, usually have two main operation modes, namely field operation and road operation. The former requires high torque traction for ploughing or harvesting, with a typical operation speed of 2–10 km/h, and the latter is in demand of a relatively high speed, with a representative speed of 25–40 km/h. It is obvious that the torque and speed requirements of these two operation modes are significantly different, which results in difficulty regarding design of PM traction motor for ETs.

Pole-changing (PC), as a conventional method to widen speed range, has been adopted in induction motors (IMs) for decades to obtain PC-IMs [9,10]. The PC armature winding of PC-IMs can be reconnected to generate armature fields with different pole-pair numbers and then couple with different induced excitation fields to realize different operation modes [11,12]. Electrical switches are used mainly to achieve winding connection transformation [13,14]. Meanwhile, electronic switches can also be adopted to change current phases and realize PC operation [15]. However, PC-IMs still suffer from inherent drawbacks, such as low torque density and low efficiency.

PC methodology has also been used in PM motors. Since the excitation and armature fields of PM motors are independent and must have the same pole-pair number to realize

effective coupling, the PM excitation field of a PC-PM motor should be able to change its pole-pair number or have two kinds of harmonics with different pole-pair numbers to couple with the armature field before and after PC. Correspondingly, two solutions can be adopted. The first one is the PM memory motor (PMMM) [16,17], in which the magnetization direction of the adopted low-coercivity-force PMs can be altered by magnetizing current. Thus, the pole-pair number of PM excitation field can be changed [18,19]. The second solution is adoption of hybrid rotors [20], in which two PM arrays with different pole-pair numbers are arranged to produce two different PM fields, named dual-harmonic field. In addition, PC operation can also be realized on field modulation PM motors, in which armature winding can be wound according to different modulated harmonics. Then, various operation modes can thus be obtained and the speed range widened [21,22].

In fact, there are harmonics in the PM field of conventional PM motors (CPMMs). Therefore, CPMMs can work as PC-PM motors in theory when PC armature winding is equipped. However, the amplitude of the PM field harmonics of CPMMs is usually much lower than that of the fundamental one; thus, the output performance of the motor will be greatly reduced when the armature winding is connected according to the pole-pair number of one of the harmonics. Therefore, a split PM topology is employed in this paper to propose a novel dual-harmonic PC motor with split PM poles (DHPCM-SPMPs) based on a nine-slot/eight-pole CPMM. In Section 2, the design principle of the DHPCM-SPMPs is introduced. In Section 3, the electromagnetic performances are analyzed by finite element analysis (FEA), which shows that the proposed motor has advantages of high torque output in the low-speed region and wide speed range based on PC operation.

2. Design Principle of DHPCM-SPMPs

2.1. Topology Design Principle

Figure 1a shows the topology of the 9-slot/8-pole CPMM. The corresponding structure parameters are shown in Table 1. Eight pieces of surface-mounted PMs are alternately magnetized radially and evenly distributed circumferentially on the rotor. The corresponding no-load air-gap flux density by finite element analysis (FEA) is shown in Figure 1b. The amplitude of the 4-pole-pair fundamental component is about 1.23 T and is much higher than those of the other harmonics. It means the PM field can be fully utilized to produce the relatively high torque output when the winding pole-pair number is 4. However, the no-load electromotive force (EMF), which is proportional to the speed, will be very high when the motor works at a high-speed condition. Therefore, the operation speed is usually limited by a determined DC-bus voltage, which leads to difficulty to adopt a CPMM directly for ETs.

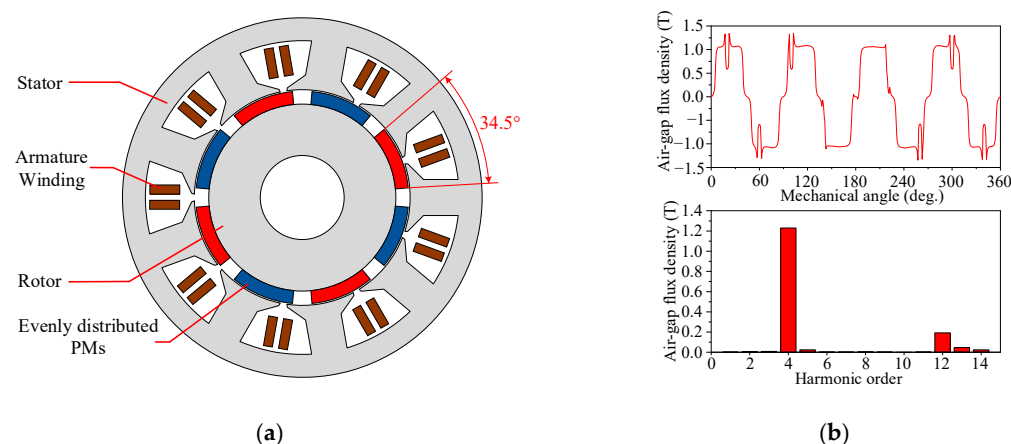


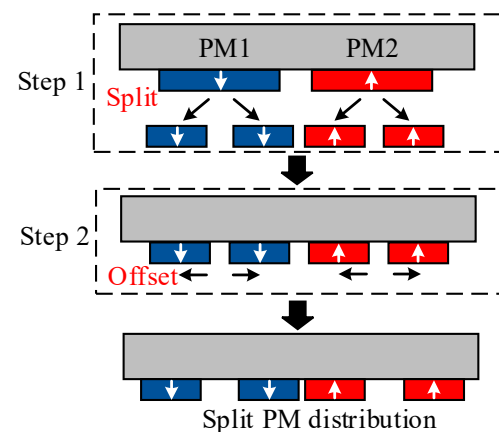
Figure 1. 9-slot/8-pole conventional PM motor: (a) motor structure; (b) air-gap flux density waveform and spectra.

Table 1. Structure parameters of the two motors.

Parameters	CPMM and DHPCM-SPMPs
Main tooth number	9
Rotor pole-pair number, P_{PM}	4
Stator outer diameter, D_{so} , mm	120
Stator inner diameter, D_{si} , mm	72
Air-gap length, g , mm	0.5
Magnet thickness, mm	4.3
Magnet volume, mm^3	68,600
Stacking length, l_a	100
Winding turns per coil, N_{coil}	35
Slot factor	0.65
Phase current, A	14
PM remanence, B_r , T	1.3
Silicon steel sheet thickness, mm	0.35

It can be seen from Figure 1b that there is also a 12-pole-pair harmonic, namely the 3rd harmonic, in the PM field of the 9-slot/8-pole CPMM. Therefore, when the armature winding is changed to connect according to the 12-pole-pair harmonic, the motor can operate as a PC-PM motor and the no-load EMF can be reduced to obtain a wider speed regulation range. However, the amplitude of the 12-pole-pair harmonic is only about 0.2 T, so the torque output capability will be greatly reduced.

To increase the amplitude of the 3rd harmonic, the PM topology is developed. The original evenly distributed PMs, taking the PM1 and PM2 as examples, as shown in Figure 2, are split into two pieces first, respectively, and are offset from each center line to form the split PM pole structure. Then, the proposed DHPCM-SPMPs can be obtained, as shown in Figure 3. The magnetized directions of the split PMs remain the same with their original ones, so the pole-pair number of the fundamental PM field is unchanged. The principle of increasing the 3rd harmonic component is discussed as follows.

**Figure 2.** The PM topology transformation process.

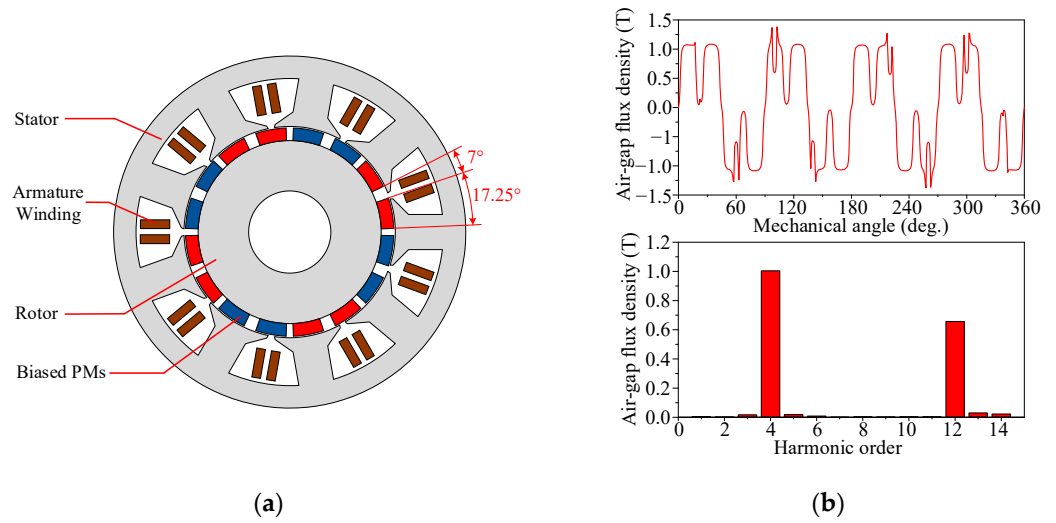


Figure 3. Dual-harmonic PC motor with split PMs. (a) Motor structure. (b) Air-gap flux density waveform and spectra.

The PM magnetomotive force (MMF) distributions of the CPMM and the proposed DHPCM-SPMPs are shown in Figure 4.

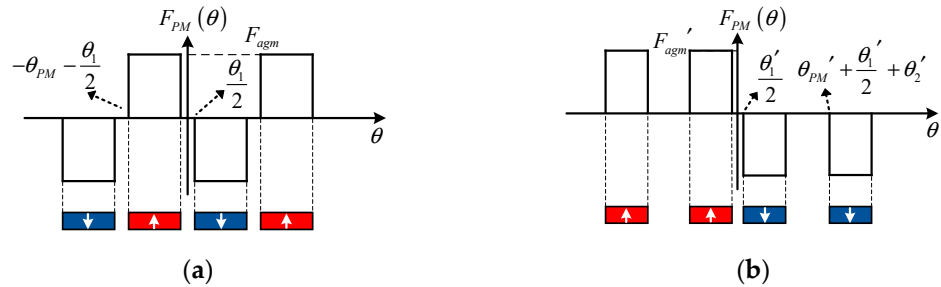


Figure 4. PM MMF distribution. (a) CPMM. (b) DHPCM-SPMPs.

The PM MMF mathematical models in Figure 4a,b can also be expressed, respectively, as

$$\begin{cases} F_{ag}(\theta, t) = \sum_{j=1,3,\dots}^{+\infty} F_{agj} \sin[jP_{PM}(\theta - \omega_m t)] \\ F_{agj} = -\frac{4F_{agm}}{j\pi} \sin\left(\frac{j\pi}{2}\right) \sin\left(\frac{jP_{PM}\theta_{PM}}{2}\right) \end{cases} \quad (1)$$

$$\begin{cases} F_{ag}'(\theta, t) = \sum_{j=1,3,\dots}^{+\infty} F_{agj}' \sin[jP_{PM}(\theta - \omega_m t)] \\ F_{agj}' = -\frac{8F_{agm}'}{j\pi} \sin\left(\frac{j\pi}{2}\right) \sin\left(\frac{jP_{PM}\theta_{PM}'}{2}\right) \cos\left(\frac{jP_{PM}(\theta_{PM}' + \theta_2')}{2}\right) \end{cases} \quad (2)$$

where $F_{ag}(\theta)$ and $F_{ag}'(\theta)$ are the PM MMF of the CPMM and DHPCM-SPMPs, respectively, F_{agj} and F_{agj}' are the amplitudes of the j th harmonic of the two motors, respectively, F_{agm} and F_{agm}' are the amplitudes of the air-gap MMF of the two motors, respectively, θ_{PM} and θ_{PM}' are the angles of each PM of the two motors, respectively, P_{PM} is the PM pole-pair number, θ_1 is the angle between adjacent PMs of the CPMM, θ_1' and θ_2' are the angles between adjacent PMs with the same and opposite magnetization directions, respectively, of the DHPCM-SPMPs, θ is the mechanical angle, ω_m is the mechanical angular speed and t is time. Thus, the amplitude ratios of the 3rd harmonic to the 1st one of the two motors can be obtained as

$$\begin{cases} \text{CPMM} : \kappa_1 = \sin\left(\frac{3P_{PM}\theta_{PM}}{2}\right) / 3 \sin\left(\frac{P_{PM}\theta_{PM}}{2}\right) \\ \text{DHPCM-SPMPs} : \kappa_2 = \lambda \kappa_1 \\ \lambda = \frac{\sin\left(\frac{3P_{PM}\theta_{PM}'}{2}\right) \sin\left(\frac{P_{PM}\theta_{PM}}{2}\right) \cos\left(\frac{3P_{PM}(\theta_{PM}' + \theta_2')}{2}\right)}{\sin\left(\frac{P_{PM}\theta_{PM}'}{2}\right) \sin\left(\frac{3P_{PM}\theta_{PM}}{2}\right) \cos\left(\frac{P_{PM}(\theta_{PM}' + \theta_2')}{2}\right)} \end{cases} \quad (3)$$

It can be seen from (3) that κ_2 is λ times κ_1 , and λ can also be expressed as

$$\begin{cases} \lambda = \frac{\sin(135\xi) \sin(90\xi) \cos\left(270\xi + \frac{3P_{PM}\theta_2'}{2}\right)}{\sin(45\xi) \sin(270\xi) \cos\left(45\xi + \frac{P_{PM}\theta_2'}{2}\right)} \\ \frac{90}{P_{PM}}(1 - \xi) \leq \theta_2' \leq \frac{180}{P_{PM}}(1 - \xi) \\ 0 < \xi \leq 1 \end{cases} \quad (4)$$

where ξ is the pole-arc coefficient.

It can be figured out from (4) that λ is always greater than 1, which makes $\kappa_1 > \kappa_2$. Therefore, the amplitude of the 3rd PM MMF harmonic can be increased by the split PM pole design.

Meanwhile, the air-gap flux density can be expressed as

$$\begin{cases} \text{CPMM} : B_{ag}(\theta, t) = F_{ag}(\theta, t) \Lambda(\theta) \\ \text{DHPCM-SPMPs} : B_{ag}'(\theta, t) = F_{ag}'(\theta, t) \Lambda(\theta) \end{cases} \quad (5)$$

where $\Lambda(\theta)$ is the permeance function, which is the same for the two motors due to the same rotor and stator structures. Therefore, the flux density amplitude of the 3rd harmonic can be increased due to the increase in the amplitude of the 3rd PM MMF harmonic.

2.2. Winding Design

In the 9-slot/8-pole DHPCM-SPMPs, the pole-pair numbers of the fundamental component and the 3rd harmonic of PM field are 4 and 12, respectively. The corresponding slot vector diagrams are shown in Figure 5. Indeed, the slot vector diagrams of the two harmonics are different. Meanwhile, the armature winding is always wound according to the slot vector diagram, which means the armature winding can be connected and reconnected based on these two different slot vector diagrams to achieve the PC operation, as shown in Figure 6, in which a winding pitch of 1 is selected.

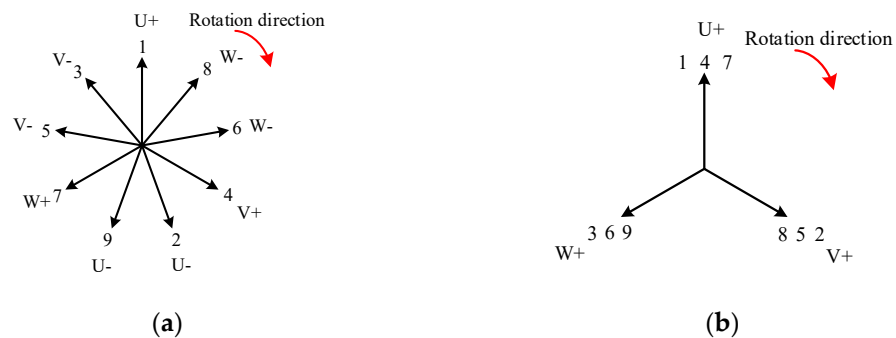


Figure 5. Slot vector diagrams. (a) 4-pole-pair number. (b) 12-pole-pair number.

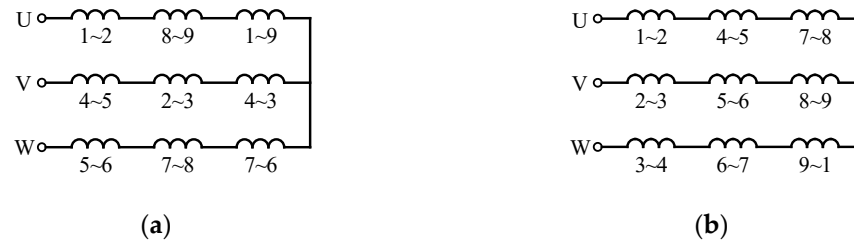


Figure 6. Winding connection. (a) For the fundamental component, 8-pole mode. (b) For the 3rd harmonic, 24-pole mode.

It can be seen from Figure 6a that, when the winding is wound according to the fundamental component, U-phase winding contains coil [1~2], [8~9] and [1~9], V-phase winding contains coil [4~5], [2~3] and [4~3], W-phase winding contains coil [5~6], [7~8] and [7~6]. By reconnecting the winding, the winding is changed to be wound according to the 3rd harmonic, where U-phase winding contains coil [1~2], [4~5] and [7~8], V-phase winding contains coil [2~3], [5~6] and [8~9], W-phase winding contains coil [3~4], [6~7] and [9~1]. The corresponding winding factors of the 8-pole and 24-pole modes are 0.945 and 0.866, respectively. In addition, winding reconnection can be realized by using electric switches, which has been used for PC-IMs.

2.3. Split PM Design

First, the torques of the two modes of ETs mentioned in Section 1 are determined by the torque outputs of the DHPCM-SPMPs, which can be expressed as

$$\begin{cases} T_I = \frac{3}{2} P_{PMI} \psi_{mI} i_s \\ T_{II} = \frac{3}{2} P_{PMII} \psi_{mII} i_s \end{cases} \quad (6)$$

where T_I and T_{II} are the torques of the 8-pole and 24-pole modes, respectively, $P_{PMI} = 4$ and $P_{PMII} = 12$ are the pole-pair numbers of the fundamental and 3rd harmonics of PM field, ψ_{mI} and ψ_{mII} are the amplitude of the PM flux linkage when the winding is wound according to the fundamental and the 3rd PM field component, respectively, i_s is the rated current and the subscripts of I and II represent the 8-pole and 24-pole modes, respectively. The ψ_{mI} and ψ_{mII} in (6) can be expressed as

$$\begin{cases} \psi_{mI}(t) = \frac{2k_{dI}k_{pI}N_{ph}l_a r_{si} B_{I\max}}{P_{PMI}} \cos\left[\frac{P_{PMI}\theta_\tau}{2} + \theta_I(t)\right] \\ \psi_{mII}(t) = \frac{2k_{dII}k_{pII}N_{ph}l_a r_{si} B_{II\max}}{P_{PMII}} \cos\left[\frac{P_{PMII}\theta_\tau}{2} + \theta_{II}(t)\right] \end{cases} \quad (7)$$

where k_{dI} and k_{dII} , k_{pI} and k_{pII} are the distribution and pitch factors in the 8-pole and 24-pole modes, respectively, N_{ph} is the turn number per phase, l_a is the stacking length, r_{si} is the stator inner radius, $B_{I\max}$ and $B_{II\max}$, $\theta_I(t)$ and $\theta_{II}(t)$ are the flux density amplitudes and phases of the 8-pole and 24-pole modes, respectively, and θ_τ is the pitch angle.

According to (3), (5), (6) and (7), the torque ratio can be expressed as

$$\frac{T_I}{T_{II}} = \frac{3k_{dI}k_{pI} \sin \frac{P_{PM}\theta_{PM}'}{2} \cos \frac{P_{PM}(\theta_{PM}' + \theta_2')}{2}}{k_{dII}k_{pII} \sin \frac{3P_{PM}\theta_{PM}'}{2} \cos \frac{3P_{PM}(\theta_{PM}' + \theta_2')}{2}} \quad (8)$$

It can be seen that the torques of the two modes are related to θ_{PM}' and θ_2 . It means, when the torque ratio of the ET is determined, the PM angle and the angle between adjacent PMs with the same magnetization direction can be determined as well. When θ_{PM}' is first determined, θ_2 can be adjusted to satisfy the torque requirements of the ET.

The torques ratio T_I/T_{II} is designed as 2.5 in this paper, which is a reasonable choice for the two-mode operation of ETs [23]. The pole-arc coefficient of the CPMM is 0.77, as shown in Figure 1a. Therefore, θ_{PM}' can first be determined when the total PM volume and

thickness in radial direction are unchanged. Then, θ_2 can be determined according to the torque ratio and (8).

As shown in Figure 3b, the air-gap flux density waveform of the DHPCM-SPMPs is changed from a square wave to a saddle-shaped wave due to the split PM pole structure. Therefore, the amplitude of the 3rd harmonic is increased to 0.64 T, which increases the output performances of the DHPCM-SPMPs when the armature winding is connected according to the 3rd harmonic. According to the corresponding parameters, λ is calculated to be 4.17, and, according to the spectra in Figures 1 and 3, the simulated λ is calculated as 4.37. It can be seen that the calculated λ by (6) and simulated λ by (7) are different by 4.6%, which shows the accuracy of the mathematical derivation and analysis.

The corresponding structure parameters of DHPCM-SPMPs are also shown in Table 1. It can be seen that the main parameters of these two motors are the same, including PM usage, except PM topology, which provides a fair comparison between the two motors in Section 3.

2.4. Speed-Widening Capability

The purpose of the PC operation in this paper is to widen the speed range. Therefore, speed-widening capability is discussed in this section.

In the d - q axis coordinate system, the speed-widening capability is related to the relative position between the characteristic current and the current limit circle, in which the current/voltage limit circle and the characteristic current can be expressed as

$$\begin{cases} i_d^2 + i_q^2 = i_s^2 \\ \left(i_d + \frac{\psi_m}{L_d}\right)^2 + i_q^2 = \left(\frac{U_{max}}{\omega_e L_d}\right)^2 \\ i_c = \frac{\psi_m}{i_d} \end{cases} \quad (9)$$

where i_d and i_q are the d -axis and q -axis currents, ψ_m is the amplitude of the PM flux linkage per phase, L_d is the d -axis inductance, U_{max} is the maximum limiting voltage, ω_e is the electrical speed and i_c is the characteristic current.

It can be seen from (9) that the characteristic current i_c is related to the PM flux linkage and winding inductance, so the PM flux linkage and winding inductance of DHPCM-SPMPs are analyzed here.

First, the PM flux linkage of one coil can be expressed as

$$\psi_{coil} = B_{imax} r_{si} l_a N_{coil} \int_{\theta_1}^{\theta_2} \cos[i\theta + \theta_i(t)] d\theta \quad (10)$$

where B_{imax} and $\theta_i(t)$ are the amplitude and phase of the i th harmonic, respectively, N_{coil} is the turn number per coil, θ_1 and θ_2 are the angular positions of the two coil sides. According to (10), the PM flux linkage amplitudes of the 8-pole and 24-pole modes can be calculated.

The winding inductance of the two modes can be calculated by the turn function and winding function. The self-inductance L_{uu} and the mutual-inductance L_{uv} can be expressed as

$$\begin{cases} L_{uu} = \mu_0 r_g l_a \int_0^{2\pi} \frac{T_u(\theta) W_u(\theta)}{g_0} d\theta \\ L_{uv} = \mu_0 r_g l_a \int_0^{2\pi} \frac{T_u(\theta) W_v(\theta)}{g_0} d\theta \end{cases} \quad (11)$$

where μ_0 is the vacuum permeability, r_g is the radius of air-gap, g_0 is the air-gap length, $T_u(\theta)$ is the turn function of U-phase, $W_u(\theta)$ and $W_v(\theta)$ are the winding functions of U-phase and V-phase, respectively. According to (11), the turn and winding functions of the two modes can be drawn as in Figure 7. The winding function waveforms of the two phases in the 8-pole and 24-pole modes are $N_{coil}/9$ and $N_{coil}/3$ lower than the turn function waveforms, respectively, due to the asymmetry of the armature MMF. Therefore, the winding inductances of the two modes are different as well according to (11).

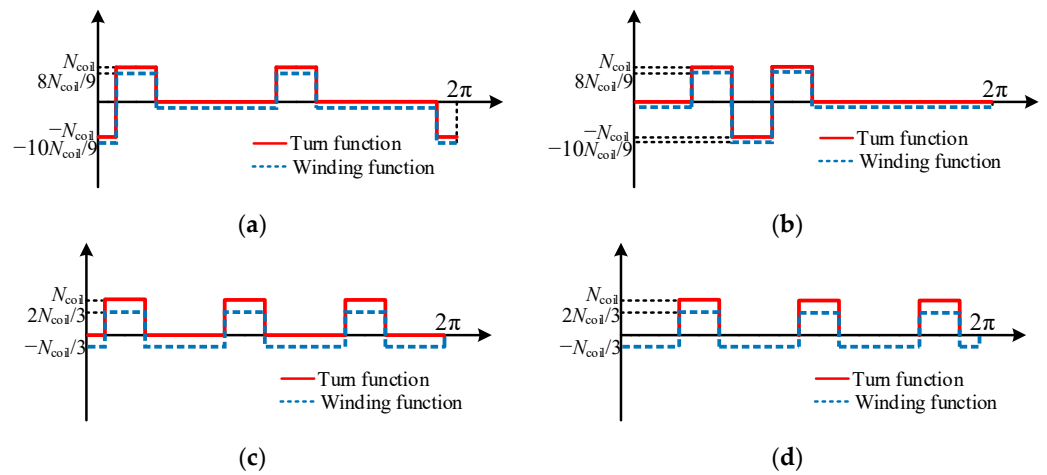


Figure 7. Turn and winding functions. (a) 8-pole mode/U-phase. (b) 8-pole mode/V-phase. (c) 24-pole mode/U-phase. (d) 24-pole mode/V-phase.

The final calculated PM flux linkage amplitudes and winding inductances are shown in Table 2. It can be seen that the PM flux linkage amplitudes of the two modes are different due to PC. Meanwhile, the self- and mutual-inductances also have a change before and after PC. Since the PM is surface-mounted on the rotor, the motor basically shows a non-salient pole characteristic. Therefore, the d-axis inductance can be calculated as $L_{uu} - L_{uv}$. Finally, the characteristic current i_c can be expressed as $\psi_m / (L_{uu} - L_{uv})$ and calculated in Table 2. It can be found that, since the PM flux linkage of 8-pole mode is much larger than that of 24-pole mode, the characteristic current of the former is significantly larger than that of the latter, although the d-axis inductances of two modes are very close.

Table 2. Calculated PM flux linkage and winding inductances.

Parameters	8-Pole Mode	24-Pole Mode
PM flux linkage amplitude, Wb	0.182	0.025
Self-inductance, mH	2.3	2.1
Mutual-inductance, mH	−0.53	−1.03
d-axis inductance, mH	2.83	3.13
Characteristic current, A	64.3	8

Then, the operation characteristic of the motor can be drawn as Figure 8. The characteristic current points of 8-pole and 24-pole modes, A_1 and A_2 , respectively, are outside and inside the current limit circle.

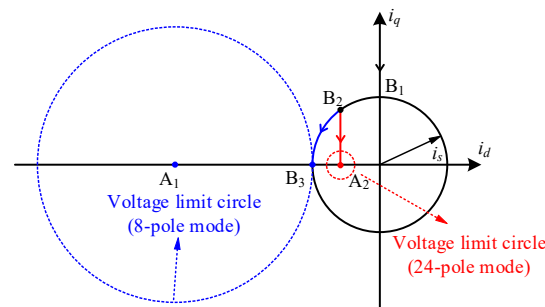


Figure 8. The operation characteristics of DHPCM-SPMPs.

According to (9), the maximum speed of 8-pole mode at B_3 can be expressed as

$$\omega_{eI} = \frac{U_{\max}}{\psi_{mI} - L_{dI}i_s} \tag{12}$$

The maximum speed of 8-pole mode is limited due to the large PM flux linkage.

On the other hand, it can be seen from Figure 7 that the voltage limit circle of 24-pole mode can be infinitely small. According to (9), the speed can be infinite in theory, which means the speed can be infinite theoretically by PC.

3. Electromagnetic Performance Analysis and Comparison

The meshed models of these two motors are shown in Figure 9. The mesh elements of the DHCPM-SPMPs and CPMM are 33,034 and 34,786, respectively, which are very close so as to ensure similar simulating accuracy.

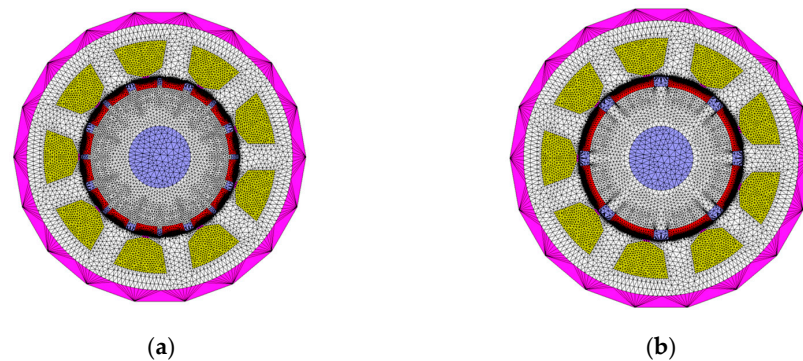


Figure 9. The meshed models. (a) DHCPM-SPMPs. (b) CPMM.

First, the simulated PM flux linkages of the two modes are shown in Figure 10. Indeed, the amplitudes of the two modes are 0.178 Wb and 0.025 Wb, respectively, which are basically consistent with the calculated ones in Table 2. Moreover, there is the third harmonic in the PM flux linkage of eight-pole mode, of which the amplitude is about 0.018 Wb. On the other hand, the flux linkage waveform of 24-pole mode is very sinusoidal.

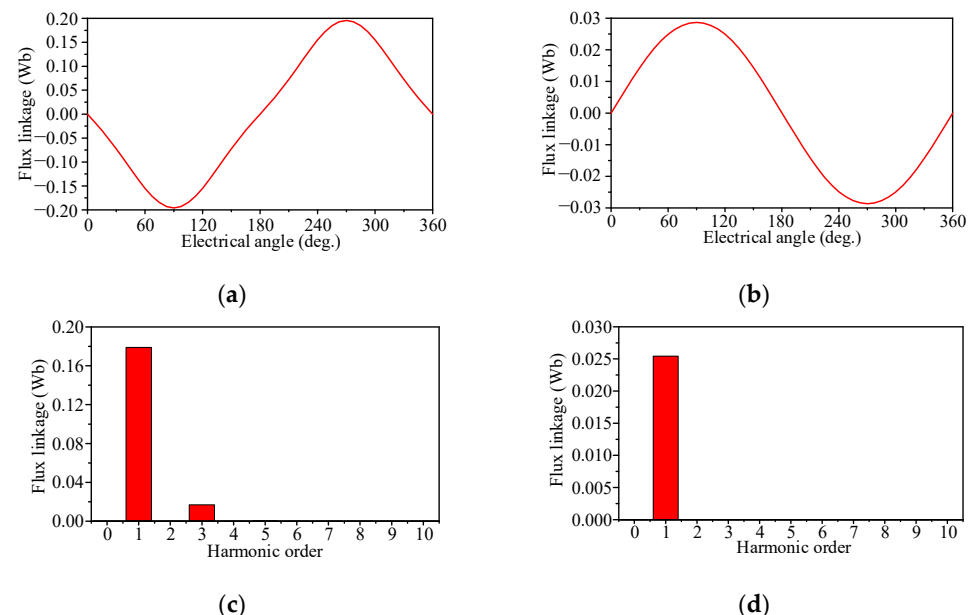


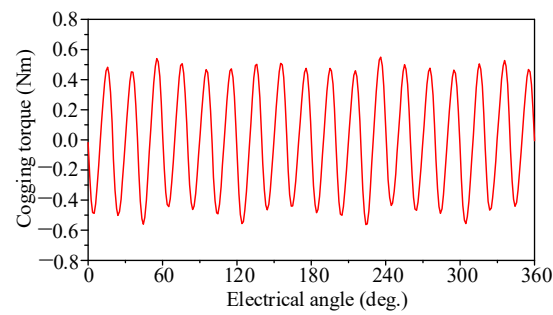
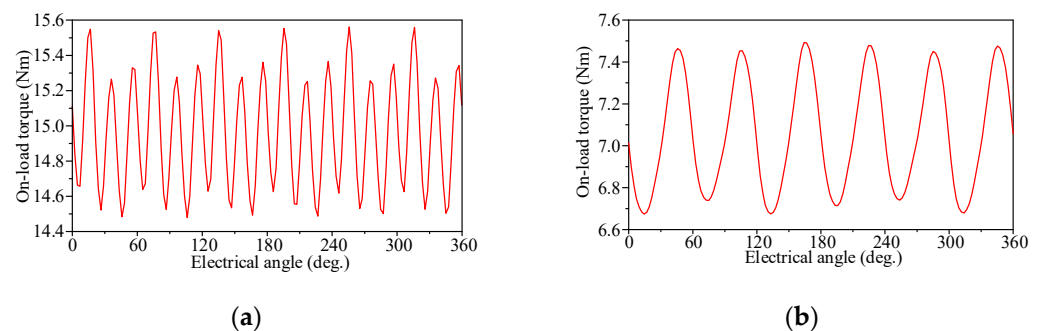
Figure 10. PM flux linkage: (a) 8-pole mode; (b) 24-pole mode. Spectrum of: (c) 8-pole mode; (d) 24-pole mode.

The simulated inductances of the two modes are shown in Table 3. The inductances by FEA are basically consistent with the calculated ones in Table 2. The characteristic currents of eight-pole mode and twenty-four-pole mode are close to the calculated ones, which shows the accuracy of the calculation.

Table 3. Inductances by FEA.

Parameters	8-Pole Mode	24-Pole Mode
Self-inductance, mH	2.2	2.4
Mutual-inductance, mH	−1	−1.1
d-axis inductance, mH	3.15	3.45
q-axis inductance, mH	3.28	3.55
Characteristic current, A	56.5	7.2

The cogging torque of the DHPCM-SPMPs is shown in Figure 11, of which the peak-to-peak value is about 1 Nm. The on-load torques of the two modes are shown in Figure 12 when the phase current of 14 A is fed by $i_d = 0$ control strategy. Evidently, the average on-load torques of the two modes are about 15 Nm and 7.1 Nm, respectively. The torque ripples of the two modes are about 7.3% and 11.3%. It should be mentioned that the simulated torque ratio of the two modes is about 13% higher than the design objective because the flux leakage is ignored in the magnetic circuit method.

**Figure 11.** Cogging torque of DHPCM-SPMPs.**Figure 12.** On-load torque of two modes. (a) 8-pole mode. (b) 24-pole mode.

To verify the speed-widening capability of DHPCM-SPMPs, the torque–speed characteristic is investigated by FEA when the bus voltage is 250 V. As shown in Figure 13, the torque–speed curve of eight-pole mode owns a high torque output of 15 Nm, while the maximum speed can only reach about 2750 rpm. The PC operation is carried out at the intersection of the two curves. Then, the operation locus is changed to the 24-pole mode one, and the maximum speed is increased to about 16,000 rpm. This speed is 8.9 times the base speed and is about 5.8 times the maximum speed in eight-pole mode.

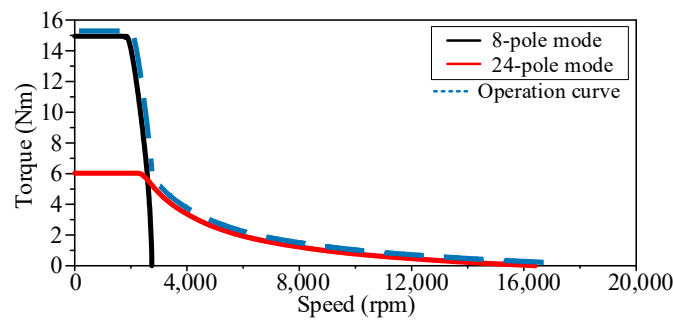


Figure 13. The torque–speed curves.

The efficiency maps of the two modes are shown in Figure 14. The maximum efficiency of eight-pole mode reaches 97.5%, while that of 24-pole mode is 91% because of the higher iron loss caused by the higher magnetic field frequency. The high efficiency area (>80%), which is the main operation region for PM motors, shows values of 89.9% and 43.4% in eight-pole and twenty-four-pole modes, whose maximum speeds can reach 2700 rpm and 5300 rpm, respectively. The envelope curves of eight-pole and twenty-four-pole modes are consistent with those in Figure 13.

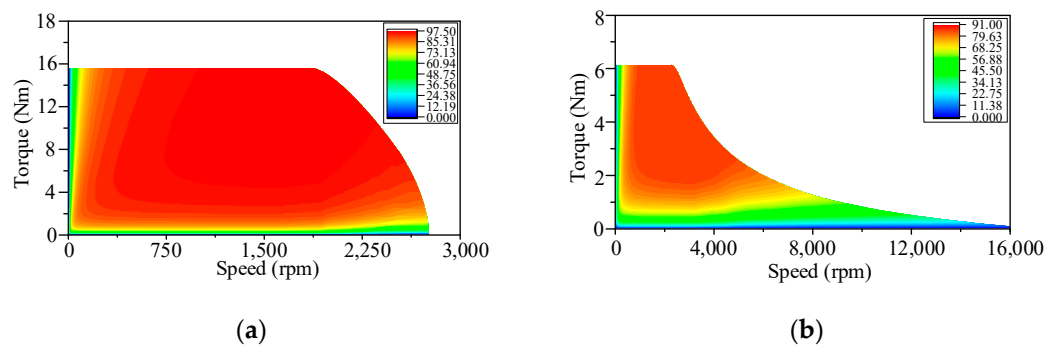


Figure 14. The efficiency maps of the two modes. (a) 8-pole mode. (b) 24-pole mode.

To indicate the fitness of the proposed motor on the ET, the operation parameters of the motor and the ET are summarized in Table 4. It should be mentioned that the transmission system is simplified as a fixed-ratio gearbox with a gear ratio of 30. The diameter of the driving wheels is 0.5 m in this paper. The maximum speed of the tractor can be increased from 17 km/h to 33 km/h by the PC operation when the motor works in high efficiency areas. The final performance parameters are shown in Table 5.

Table 4. Operation parameters of DHPCM-SPMPs and ET.

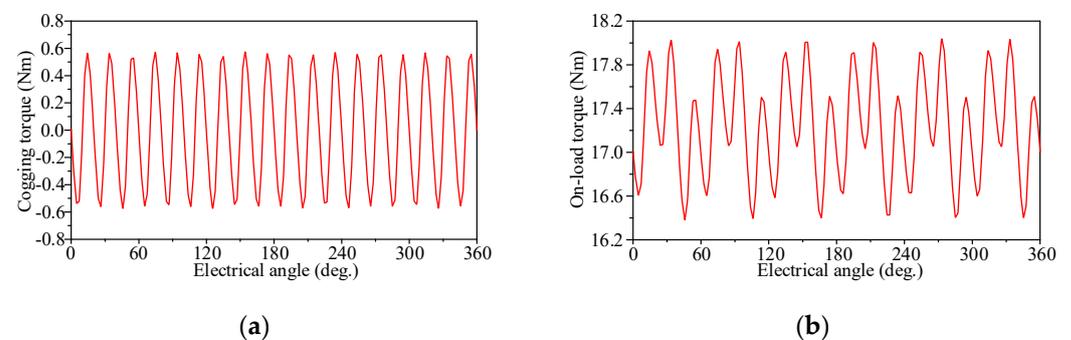
Mode	Motor		Tractor
	Speed Range	Maximum Efficiency	Speed Range
8-pole	220–2700 rpm	97.5%	1.4–17 km/h
24-pole	630–5300 rpm	91%	4–33 km/h

Table 5. Performance parameters of DHPCM-SPMPs.

Parameters	DHPCM-SPMPs	
	8-Pole Mode	24-Pole Mode
Average Torque, Nm	15	7.1
Torque per volume, kNm/m ³	13.2	6.3
PM volume, mm ³		68,600
Torque per PM, kNm/m ³	218	103
Current density, A/mm ³		5
Efficiency @250 V	97.5%	91%
Maximum speed @250 V, rpm	2750	16,000

To demonstrate the advantages of the proposed DHPCM-SPMPs, it is compared with the CPMM in Figure 1a. As mentioned before, the main structure parameters of the two motors except PM topology are the same to carry out a reasonable comparison.

First, the torque performance of the CPMM is calculated by FEA and shown in Figure 15. It can be seen from Figure 15a that the peak-to-peak value of the cogging torque is about 1.1 Nm, which is 0.1 Nm higher than that of DHPCM-SPMPs. The average on-load torque shown in Figure 15b is about 17.1 Nm, which is 2.1 Nm higher than that in eight-pole mode of DHPCM-SPMPs. This is due to the higher fundamental component of PM flux density, which is about 1.2 T in Figure 1b, while the fundamental component of PM flux density is reduced to about 1 T because of the adopted split PM pole design in the DHPCM-SPMPs. However, the torque density in eight-pole mode of DHPCM-SPMPs reaches 13.2 kNm/m³, as shown in Table 5, which is still high. The torque ripple of the CPMM is about 9.4%, which is a little higher than that of eight-pole mode of the proposed motor.

**Figure 15.** Torque performance of CPMM. (a) Cogging torque. (b) On-load torque.

The efficiency map of the CPMM is shown in Figure 16. The maximum efficiency of CPMM is 96.5%, which is lower than that of DHPCM-SPMPs in eight-pole mode, and the high efficiency area (>80%) of CPMM is about 85%. Although the maximum torque output of CPMM is higher, the speed range is limited. As can be seen in Figure 17, the maximum speed of DHPCM-SPMPs can reach 16,000 rpm, which is about 5.8 times the maximum speed of CPMM. Meanwhile, although the CPMM owns a high torque output area as Region 1, DHPCM-SPMPs also has an extra area as Region 2, which is much larger than the former. Region 2 benefiting from PC operation makes DHPCM-SPMPs own a much wider speed range.

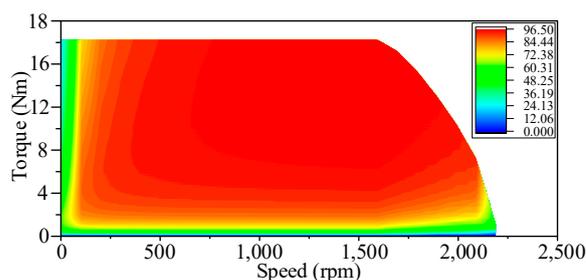


Figure 16. The efficiency map of CPMM.

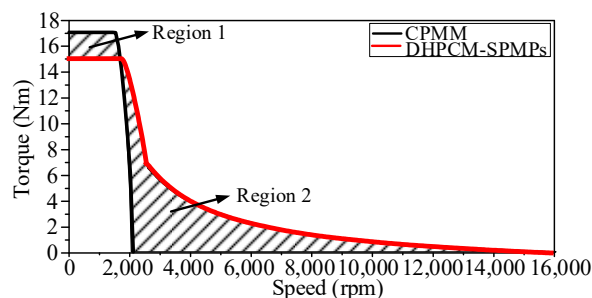


Figure 17. Torque–speed curves of the two motors.

4. Conclusions

In this paper, a novel nine-slot/eight-pole DHPCM-SPMPs is proposed. First, the design principle of DHPCM-SPMPs is introduced. The split PM pole structure is adopted so that the amplitude of the third harmonic of PM flux density is increased to improve the output capability of 24-pole mode. Then, the electromagnetic performance of DHPCM-SPMPs is analyzed by FEA, which demonstrates high torque capability in eight-pole mode and wide speed range in twenty-four-pole mode. The efficiency maps show that the maximum efficiencies of eight-pole and twenty-four-pole modes can reach 97.5% and 91%. In addition, the operation parameters of the proposed motor and an ET are summarized, which show the fitness of the motor on the ET. Finally, the DHPCM-SPMPs is compared with the CPMM. The results show that the maximum speed of the proposed can be increased by 5.8 times by PC operation.

Author Contributions: Investigation, J.Z. and M.K.; Methodology, Y.S.; Supervision, Y.D.; Writing—original draft, Z.H. All authors have read and agreed to the published version of the manuscript.

Funding: This research is funded by National Natural Science Foundation of China (52177045) and by Jiangsu Agriculture Science and Technology Innovation Fund (CX(21)3147).

Conflicts of Interest: The authors declare no conflict of interest.

References

- Troncon, D.; Alberti, L. Case of Study of the Electrification of a Tractor: Electric Motor Performance Requirements and Design. *Energies* **2020**, *13*, 2197. [[CrossRef](#)]
- Baek, S.Y.; Kim, Y.S. Development and Verification of a Simulation Model for 120 kW Class Electric AWD (All-Wheel-Drive) Tractor during Driving Operation. *Energies* **2020**, *13*, 2422. [[CrossRef](#)]
- Mocera, F.; Soma, A. Analysis of a Parallel Hybrid Electric Tractor for Agricultural Applications. *Energies* **2020**, *13*, 3055. [[CrossRef](#)]
- Zhang, L.; Zhu, X.; Cui, R.; Han, S. A Generalized Open-Circuit Fault-Tolerant Control Strategy for FOC and DTC of Five-Phase Fault-Tolerant Permanent-Magnet Motor. *IEEE Trans. Ind. Electron.* **2022**, *69*, 7825–7836. [[CrossRef](#)]
- Zhou, X.; Zhu, X.; Wu, W.; Xiang, Z.; Liu, Y.; Quan, L. Multi-objective Optimization Design of Variable-saliency-ratio PM Motor Considering Driving Cycles. *IEEE Trans. Ind. Electron.* **2021**, *68*, 6516–6526. [[CrossRef](#)]
- Xu, L.; Zhu, X.; Wu, W.; Fan, W.; Zhou, X.; Cai, X.; Quan, L. Flux-leakage Design Principle and Multiple-operating Conditions Modeling of Flux Leakage Controllable PM Machine Considering Driving Cycles. *IEEE Trans. Ind. Electron.* **2022**, *69*, 8862–8874. [[CrossRef](#)]
- Xu, L.; Zhu, X.; Fan, W.; Zhang, C.; Zhang, L.; Quan, L. Comparative Analysis and Design of Partitioned Stator Hybrid Excitation Axial Flux Switching PM Motors for In-wheel Traction Applications. *IEEE Trans. Energy Convers.* **2022**, *37*, 1416–1427. [[CrossRef](#)]

8. Huynh, T.A.; Hsieh, M.F. Performance Analysis of Permanent Magnet Motors for Electric Vehicles (EV) Traction Considering Driving Cycles. *Energies* **2018**, *11*, 1385. [[CrossRef](#)]
9. Osama, M.; Lipo, T.A. Modeling and Analysis of a Wide-speed-range Induction Motor Drive based on Electronic Pole Changing. *IEEE Trans. Ind. Appl.* **1997**, *33*, 1177–1184. [[CrossRef](#)]
10. Latif, T.; Husain, I. Design and Analysis of an Induction Motor for an Enhanced Constant Power Region with Electronic Pole Changing. In Proceedings of the 2021 IEEE International Electric Machines & Drives Conference (IEMDC), Hartford, CT, USA, 17–20 May 2021; pp. 1–6.
11. Mallampalli, S.; Zhu, Z.Q.; Mipo, J.C.; Personnaz, S. Six-Phase Pole-Changing Winding Induction Machines with Improved Performance. *IEEE Trans. Energy Convers.* **2021**, *36*, 534–546. [[CrossRef](#)]
12. Ge, B.; Sun, D.; Wu, W.; Peng, F.Z. Winding Design, Modeling, and Control for Pole-Phase Modulation Induction Motors. *IEEE Trans. Magn.* **2013**, *49*, 898–911. [[CrossRef](#)]
13. Kume, T.; Iwakane, T.; Sawa, T.; Yoshida, T.; Nagai, I. A Wide Constant Power Range Vector-controlled AC Motor Drive using Winding Changeover Technique. *IEEE Trans. Ind. Appl.* **1991**, *27*, 934–939. [[CrossRef](#)]
14. Ismail, K.S. A New Graphical Approach to Three Phase Two Speed Induction Motor Winding Design. *IEEE Trans. Energy Convers.* **1998**, *13*, 334–346. [[CrossRef](#)]
15. Osama, M.; Lipo, T.A. Experimental and Finite Element Analysis of an Electronic Pole-Change Drive. In Proceedings of the 1999 IEEE Industry Applications Conference, Thirty-Forth IAS Annual Meeting, Phoenix, AZ, USA, 3–7 October 1999; pp. 914–921.
16. Ostovic, V. Pole-Changing Permanent-Magnet Machines. *IEEE Trans. Ind. Appl.* **2002**, *38*, 1493–1499. [[CrossRef](#)]
17. Li, F.; Chau, K.T.; Liu, C.; Zhang, Z. Design Principles of Permanent Magnet Dual-Memory Machines. *IEEE Trans. Magn.* **2012**, *48*, 3234–3237. [[CrossRef](#)]
18. Li, F.; Chau, K.T.; Liu, C.; Qiu, C. New Approach for Pole-Changing with Dual-Memory Machine. *IEEE Trans. Appl. Supercond.* **2014**, *24*, 2291296. [[CrossRef](#)]
19. Lee, J.H.; Lee, S.C.; Lee, T.H. Characteristics Analysis in a Pole Changing Memory Motor using Coupled FEM & Preisach Modeling. In Proceedings of the Digests of the 2010 14th Biennial IEEE Conference on Electromagnetic Field Computation, Chicago, IL, USA, 9–12 May 2010; p. 1.
20. Ghoroghchian, F.; Aliabad, A.D.; Amiri, E. Two-speed Line Start Permanent Magnet Synchronous Motor with Dual Magnetic Polarity. *IEEE Trans. Ind. Appl.* **2018**, *54*, 4268–4277. [[CrossRef](#)]
21. Du, Y.; He, Z.; Zhu, X.; Xiao, F.; Zhang, C.; Xu, L.; Zuo, Y.; Quan, L. A Novel Pole-changing Permanent Magnet Vernier Motor. *IEEE Trans. Ind. Electron.* **2022**. [[CrossRef](#)]
22. Du, Y.; Mao, Y.; Xiao, F.; Zhu, X.; Sun, Y.; Quan, L. A Pole-Changing Doubly Salient Permanent Magnet Motor. *IEEE Trans. Transp. Electrification* **2022**, *8*, 2479–2489. [[CrossRef](#)]
23. Chen, Y.N.; Xie, B.; Du, Y.F.; Mao, E.R. Powertrain Parameter Matching and Optimal Design of Dual-motor Driven Electric Tractor. *Int. J. Agric. Biol. Eng.* **2019**, *12*, 33–41. [[CrossRef](#)]